Materials Science & Engineering C 118 (2021) 111401

Contents lists available at ScienceDirect

Materials Science & Engineering C

journal homepage: www.elsevier.com/locate/msec

Photoluminescence label-free immunosensor for the detection of Aflatoxin B1 using polyacrylonitrile/zinc oxide nanofibers

Valerii Myndrul[a], Emerson Coy[a], Mikhael Bechelany[b], Igor Iatsunskyi[a,*]

[a] NanoBioMedical Centre, Adam Mickiewicz University, 3, Wszechnicy Piastowskiej Str., 61-614 Poznan, Poland
[b] Institut Européen des Membranes, IEM, UMR 5635, Univ Montpellier, ENSCM, CNRS, 34095 Montpellier CEDEX 5, France

ARTICLE INFO

Keywords:
ZnO
Immunosensor
Detection
Aflatoxin B1
Photoluminescence

ABSTRACT

The precise and rapid detection of hazardous molecules, microorganisms, pollutants, and toxins currently remains a global challenge. Aflatoxin B1 (AFB1) is a toxic and dangerous product of fungi that considered as cancerogenic, mutagenic, and immunosuppressive for humans and animals. Therefore, the screening of AFB1 in food and beverages plays an important role in preventing foodborne illnesses. In this study, AFB1 molecules were detected in a microfluidic device with integrated polyacrylonitrile/zinc oxide (PAN/ZnO) nanofibers fabricated via a combination of the electrospinning, and atomic layer deposition (ALD) techniques. The structural and optical analyses of PAN/ZnO nanofibers were performed and samples with the most suitable properties were utilized for AFB1 detection. In order to obtain the biorecognition layer towards AFB1, PAN/ZnO samples were modified by (3-Aminopropyl) triethoxysilane (APTES), and glutaraldehyde (GA), bovine serum albumin (BSA) and monoclonal antibodies (Anti-AFB1). Subsequently, photoluminescence (PL)-based immunosensor was integrated into a microfluidic cell and tested for AFB1 detection. The mechanism of PL changes caused by AFB1 & Anti-AFB1 complex formation was analyzed and developed. The proposed approach enables the detection of AFB1 with the lowest concentration (LOD) of about 39 pg/ml, while the sensitivity range was evaluated as 0.1–20 ng/ml. The obtained values of LOD and sensitivity, as well as the simplicity of the detection method, make this approach a prospect for further application.

1. Introduction

Mycotoxins are dangerous secondary metabolites produced by some organisms from the kingdom fungi. Generally, they can be released to the foodstuff during the fungi growth, especially in humid and warm conditions [1,2]. Moreover, they have been classified as possible carcinogens and immunosuppressive agents [3,4]. Therefore, precise control and detection of mycotoxins in human and animal rations can help to avoid their negative influence on the general health.

Despite the thorough monitoring of mycotoxin levels in food and beverages within the European Union, contaminated foodstuffs still have been delivered to the customers. Adegbeye et al. have reported on the current situation of foodstuff contamination by mycotoxins, and indeed it takes place worldwide, especially in the developing countries [5]. Furthermore, Global Climate Change could promote the spread of mycotoxins in Europe [5].

Among different mycotoxins, Aflatoxin B1 (AFB1) has been found to be one of the most food-contaminating toxins [6]. Being in the human liver, AFB1 stimulates cellular metabolism to generate high levels of reactive oxygen species (ROS) and free radicals. Such conditions lead to cell death, hepatotoxicity and initiate human hepatocellular carcinoma [7]. Based on the mentioned above, it is important to develop a high-sensitive and simple approach for AFB1 detection.

Traditional approaches for AFB1 detection, such as chromatography methods, have a high sensitivity and specificity, but they require an expensive equipment and specially trained staff, which increase the costs of analysis [8,9]. Moreover, AFB1 detection usually requires additional secondary labeled antibodies that make this approach more complicated and expensive [1]. Due to the small size of AFB1 molecules, it can be even undetectable by the Surface Plasmon Resonance based approach (SPR), which is considered to be the most sensitive label-free techniques. In order to solve this problem the “weighting agents” such as bovine serum albumin (BSA) has been used [10]. However, BSA weighting agents can adversely affect detection selectivity; therefore, the use of highly selective receptors (for example, nanobodies against AFB1) is preferred over the AFB1-BSA using [11]. Besides, a very limited number of studies represented a general mechanism for AFB1 detection that may clarify the behavior and response

* Corresponding author.
E-mail address: igoyat@amu.edu.pl (I. Iatsunskyi).

https://doi.org/10.1016/j.msec.2020.111401
Received 17 May 2020; Received in revised form 13 August 2020; Accepted 19 August 2020
Available online 22 August 2020

during the AFB1 binding. The well-studied mechanism of detection will clarify the nature of the "detection platform-AFB1" interaction. Therefore, the major *challenge* is to develop a high-sensitive biosensing platform and/or a detection approach with a significantly reduced cost, when compared to traditional methods, and with a relative simplicity for application.

Among different types of biosensor transducers, the optical ones are small size, portable, and high precision devices. Currently, optical transducers have been successfully used in SPR, surface-enhanced Raman spectroscopy (SERS), reflectance, and photoluminescence (PL) biosensors [12]. Among optical transducers, PL - based biosensors are considered to be one of the most promising approaches, but stable, efficient and environment-friendly transducers are still required [13]. The change in the PL signal (e.g. relative PL intensity, the shape of PL curve) of semiconductors, as a function of the analyte concentration, can be used as an indicator for the detection of target molecules by the probe. The PL of semiconductors is very sensitive to small modifications of their surface (e.g. absorption of molecules on the surface) that enables to distinguish analyte concentration changes [14–20].

Nanostructured zinc oxide (ZnO) is the one of most attractive materials for PL biosensors due to high active surface area, strong room-temperature (RT) PL in the UV/VIS range [21], and high isoelectric point/IEP (pH = 9) suitable for the direct immobilization of low IEP acidic proteins or DNA via electrostatic interaction [22]. ZnO – based PL biosensors have been successfully applied for the detection of *Salmonella* [23], Ochratoxin A [17], and for the protein–protein biorecognition, etc. [19,21]. Recent discoveries show that the morphology and structural properties of ZnO are crucial for the efficient biosensor performance [24,25]. The comparison analysis of the ZnO surface topography (nanoparticles (NPs), nanorods (NRs), nanosheets (NSs) and nanobeams (NBs)) on the protein adsorption process showed that 1D ZnO nanostructures provided a higher number of surface adsorption sites [24,25]. Thus, to enhance the sensitivity of ZnO based biosensors, a high surface-to-volume ratio, such as the one present in a 1D structure, is needed.

Recently, it was proposed a novel approach to produce 1D ZnO nanostructures with a high surface architecture. This approach is based on the combination of two experimental techniques: electrospinning and atomic layer deposition (ALD) [26,27]. Electrospinning is a low-cost powerful technique, which can produce 1D organic or polymer nanofibers [28]. Electrospinning deposited 1D organic nanofibers, such as collagen, polyacrylonitrile (PAN), polylactic acid (PLA), gelatin, collagen, hyaluronic acid (HA) are widely used in tissue engineering and medicine as 3D scaffolds for cell growing [29]. At the same time, these nanofibers can be a template for PL biosensors via ALD coatings with a photonic material (e.g. ZnO based coatings). It is known that, ALD is one of the most versatile methods for fabrication of ZnO nanostructures [30]. It does not depend on the substrate geometry and can be applied for both planar samples, and porous media at relatively low temperatures [31,32]. This method provides a conformal coating of the substrate and allows the control of thickness and chemical composition of the deposited layers. In recent works, it was also demonstrated that 1D PAN/ZnO nanofibers produced by this approach can be used as an effective PL biosensor for volatile organic compounds (VOC) [27]. However, there are still several questions need to be solved: *(i)* what are the mechanisms for PL detection in ZnO; and *(ii)* is it possible to use this nanocomposite for mycotoxin (AFB1) detection.

In the present study, we report on the development of PAN/ZnO nanocomposites that can be applied for a low-cost, label-free and sensitive PL biosensor (immunosensor) towards AFB1 as a model molecule. The ZnO layer was produced by ALD technique. As a biorecognition layer, the antibody towards AFB1 (anti-AFB1) has been chosen. Structural and optical properties of the fabricated PAN/ZnO nanocomposites have been investigated by scanning electron spectroscopy (SEM), transmission electron microscopy (TEM), X-Ray diffraction analysis (XRD), Fourier-transform infrared spectroscopy (FTIR) and confocal microscopy. The PL of PAN/ZnO nanocomposites functionalized with the anti-AFB1, as well as the control samples (without anti-AFB1), was measured for different concentrations of AFB1. It was found that high surface to volume ratio of PAN/ZnO nanocomposites and high affinity of immobilized anti-AFB1 to AFB1 give the possibility of detecting AFB1 in a wide sensitivity range 0.1–20 ng/ml and with detection limit (LOD) of 39 pg/ml. Furthermore, estimated values of power coefficient, and change of Gibbs free energy indicate strong electrostatic interaction between biosensor and the analyte (AFB1). The general mechanism of the PL biosensor response change during the PAN/ZnO/APTES/GA/Anti-AFB1&AFB1 complex formation was proposed. Hereby, we propose a novel PL-based approach for AFB1 detection on PAN/ZnO/APTES/GA/Anti-AFB1 structure.

2. Experimental section

2.1. Materials

Polyacrylonitrile PAN (Mw = 150,000), and dimethylformamide (DMF) (ACS reagent, ≥99.8%) were purchased from Sigma Aldrich. Diethyl zinc (DEZ) ($Zn(CH_2CH_3)_2$, 95% purity, CAS: 557-20-0), was purchased from Sterm Chemical. Anti-AFB1 monoclonal antibodies (1 mg/ml, mouse IgG1 isotype, № A9555), AFB1 (2 μg/ml in acetonitrile, analytical standard, №34029), Protein A (№ P3838), BSA, (purity ≥98.0%, № 05470), (3-Aminopropyl)triethoxysilane (APTES, purity ≥98%), and glutaraldehyde (GA, 50 wt% in H_2O) were purchased from Sigma Aldrich. Phosphate-buffered saline (PBS, pH 7.4) was used as the diluent for AFB1 dissolution. Al biological components were diluted on the day of the experiment (without additional storage in dissolvent).

The quartz microfluidic cell (useable optic range: 170–2700 nm, v = 600 μl, w = 8 mm, d = 2 mm, h = 40 mm) was purchased from Starna Cells. The diameter of the inlet and outlet tubes was 0.9 mm (inner diameter: 0.36 mm).

2.2. PAN fiber fabrication

Polyacrylonitrile (10 wt% PAN) was dissolved in DMF. The polymer solution was kept under stirring for 1 h with the following heating in an oil bath at 80 °C for 10 min. A home-made electrospinning machine with HPx 600 605 generator (physical instruments) and a KDS 100 syringe pump was used for the electrospinning deposition process. The solution was electrospun under an applied voltage of 25 kV with a flow rate of 3 mlh^{-1} using a 0.7 mm diameter syringe (connected to the positive output of the generator) in ambient air atmosphere. The collector, made of aluminum foil was fixed at the distance of 25 cm from the tip of the syringe and was connected to the negative output of the generator. The liquid was extruded from the spinneret to produce a pendant droplet that followed the Taylor cone formation due to the electrostatic repulsion among the surface charges upon electrification. The charged jet underwent stretching and thinning under the whipping instability and solidifies quickly into a fiber with tailored diameter.

2.3. ALD of ZnO

ZnO thin layers were deposited over the PAN nanofibers by a home-made ALD set-up at 100 °C and sequential exposures to diethyl zinc (DEZ) and deionized water, separated by a purge with dry Argon (flow rate of 100 sccm). The deposition protocol included the following steps: i) 0.3 s pulse of DEZ, 30 s exposure and 50 s purge with dry Ar; ii) 2 s pulse of H_2O, 40 s of exposure, and 60 s purge with dry Ar. The growth rate was generally 2.1 Å/cycle for ZnO. The ZnO thickness growth per cycle was controlled by measuring the ZnO film's thickness on planar Si substrates placed in the reactor and proved by transmission electron microscopy on PAN nanofibers. After the ALD of ZnO over the PAN nanofibers were obtained, samples with different ZnO thicknesses were obtained: PAN/ZnO_{5nm}, PAN/ZnO_{10nm}, PAN/ZnO_{20nm}, PAN/ZnO_{50nm}.

2.4. Characterization techniques

Morphology of the PAN/ZnO nanocomposite surface was investigated by scanning electron microscopy (SEM) (JEOL, JSM7001F) with an energy dispersive X-ray (EDX) analyzer and transmission electron microscopy (TEM) (JEOL ARM 200F) high-resolution transmission electron microscope (200 kV) with an EDX analyzer. The structural state of PAN/ZnO was analyzed by means of X-ray diffraction (XRD) (PANalytical, X'pert^{3}pro MRD diffractometer) working with a Cu lamp (λ = 1.5418 Å). The Fourier-transform infrared (FTIR) spectra were obtained with the Jasco FT/IR 4700 – Fourier Transform Infrared Spectrometer. Photoluminescence was generated by a He—Cd laser (325 nm) and the emission spectra were recorded in the range from 360 to 800 nm by Ocean Optics Spectrometer USB4000. Two-photon laser fluorescence confocal microscopy (Zeiss LSM 780, the Coherent Chameleon laser with an excitation wavelength of 700 nm) was used to study the real-time PL during AFB1 adsorption.

2.5. The evaluation of PL signal of immunosensor

To prepare the biorecognition layer, the immobilization of antibodies towards AFB1 (anti-AFB1) was accomplished by the protocol described in the reference [14]. Briefly, the PAN/ZnO_{20nm} samples were functionalized by APTES, and then, after GA activation, anti-AFB1were conjugated to the surface. Finally, the Bovine BSA PBS solution was added to block the remaining active sites and to improve the selectivity of the biosensor. As a result, PAN/ZnO_{20nm}/APTES/GA/Anti-AFB1 structure was formed.

It also was supposed to add the Protein A (Prot.A) during the functionalization process to achieve oriented Anti-AFB1 immobilization, however, this step does not lead to the correct PAN/ZnO_{20nm}/APTES/GA/Prot.A/Anti-AFB1 assembly. The possible reason for the incorrect assembly can be associated with the weak binding affinity of Prot.A to anti-AFB1 antibodies [33].

Analytical characterization of the biosensor based on PAN/ZnO_{20nm}/APTES/GA/Anti-AFB1 structures was performed in a microfluidic cell (Fig. 1a, b) with the analyte flow rate about 37 ml/min. The cell was equipped with an inlet and outlet for analyte infusion. PL was excited with He—Cd (λ = 325 nm) and collected by optical fiber spectrometer using multimode optical fibers equipped with semi-spherical lenses. An output laser power was around 1–2 mW. Before measurements, 600 μl of buffer solution were pumped through the cell by using a peristaltic pump. The PL spectra of the sample were collected every 10 s. The sample was stored in a buffer solution until the PL signal reached equilibrium. Then, 600 μl of various AFB1 concentrations were subsequently infused to the cell via pumping. Biosensing tests were performed in the concentration range of 0.1–100 ng/ml (AFB1 molecules). Since all AFB1 concentrations were sequentially infused into the microfluidic cell, we assume that it would lead to the accumulation of AFB1 on the surface of ZnO.

3. Results and discussion

3.1. Structural and optical properties

In order to investigate the structure, surface morphology and optical properties of fabricated PAN/ZnO nanofibers with different ZnO thicknesses, SEM, TEM, XRD, EDX, and PL analysis were performed. Fig. 2 shows SEM images of PAN/ZnO nanocomposites with different numbers of ALD cycles (25 to 250) corresponding to different layer thicknesses. It was confirmed that applying both techniques one was able to produce PAN/ZnO nanofibers with tuned structural parameters and optical properties [26]. Fig. 2(a–c) indicate the solid "spaghetti-like" morphology with an average fiber diameter of 500 nm. Fig. 2(d–f) show the crystalline structure of ZnO layers with the visually evaluated crystallites with the size around 15–30 nm. Moreover, Fig. 2d indicates the core-shell structure with a clear border between the core (PAN polymer) and the shell (ZnO crystalline layer).

In order to confirm the ZnO conformal layer TEM experiments were conducted. Fig. 3 shows the TEM images of PAN/ZnO nanofibers: PAN/ZnO_{50nm} (Fig. 3a, b, d) and PAN/$ZnO_{20\ nm}$ (Fig. 3c, e, f). The TEM image (Fig. 3a) shows a uniform fiber with the conformal ZnO layer. TEM images (Fig. 3a–c) show the single fibers with an approximate diameter of 400–500 nm. Fig. 3d–f shows the crystalline structure of the ZnO layer over PAN fiber with an average crystallites size of about 10–15 nm. Besides, Fig. 3f represents (101) lattice plane with the interplanar distance of 0.24 nm suggest the stabilization of the wurtzite phase of ZnO. High-resolution TEM proves the polycrystalline nature of produced ALD ZnO layers for all samples.

To confirm the crystalline phase of the obtained PAN/ZnO nanofibers, XRD analysis has been also performed (Fig. 4a). The peaks at 2θ = 31.74° (001), 2θ = 34.42° (002), 2θ = 36.22° (101), and 2θ = 47.53° (102) confirm ZnO wurtzite structure [27]. The XRD peak at 2θ = 17° directly corresponds to PAN fiber [27]. It is clearly seen that the crystallinity of the PAN/ZnO_{5nm} structure is weak and the ZnO coverage which is attributed to the small amount of material, the miss orientation of the fibers towards the Bragg-Brentano condition and the polycrystallinity of the films [34]. With the growth of the ZnO layer

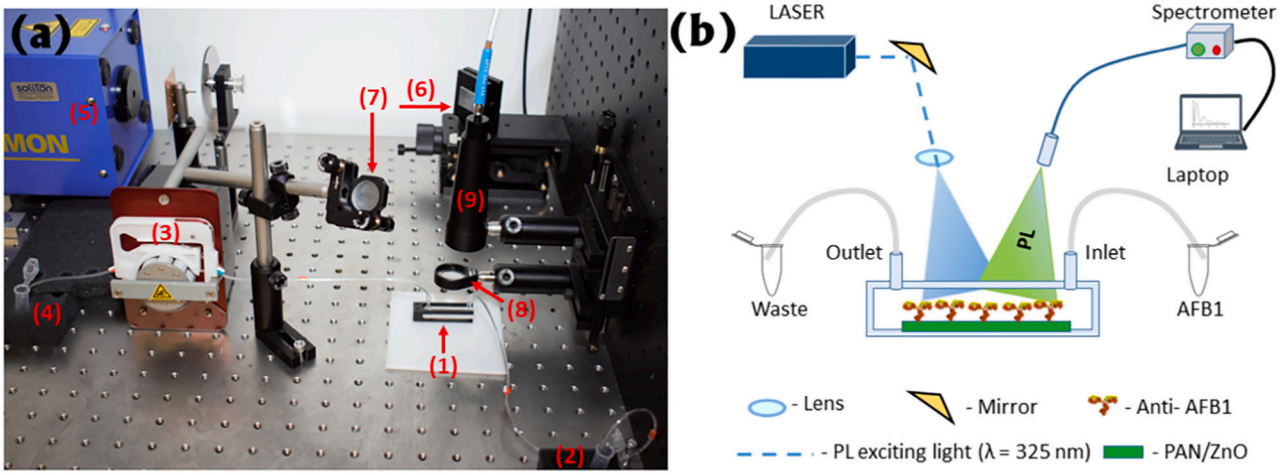

Fig. 1. (a) Photography of the experimental set-up, where (1) - microfluidic cell with tubes; (2) -AFB1 sample; (3) - peristaltic pump; (4) - AFB1 waste; (5) - laser; (6), (7) and (8) - system of mirrors and lens, (9) - light collector. (b) Scheme of the experimental set-up for the PL – based AFB1 detection on PAN/ZnO_{20nm}/APTES/GA/Anti-AFB1 structure.

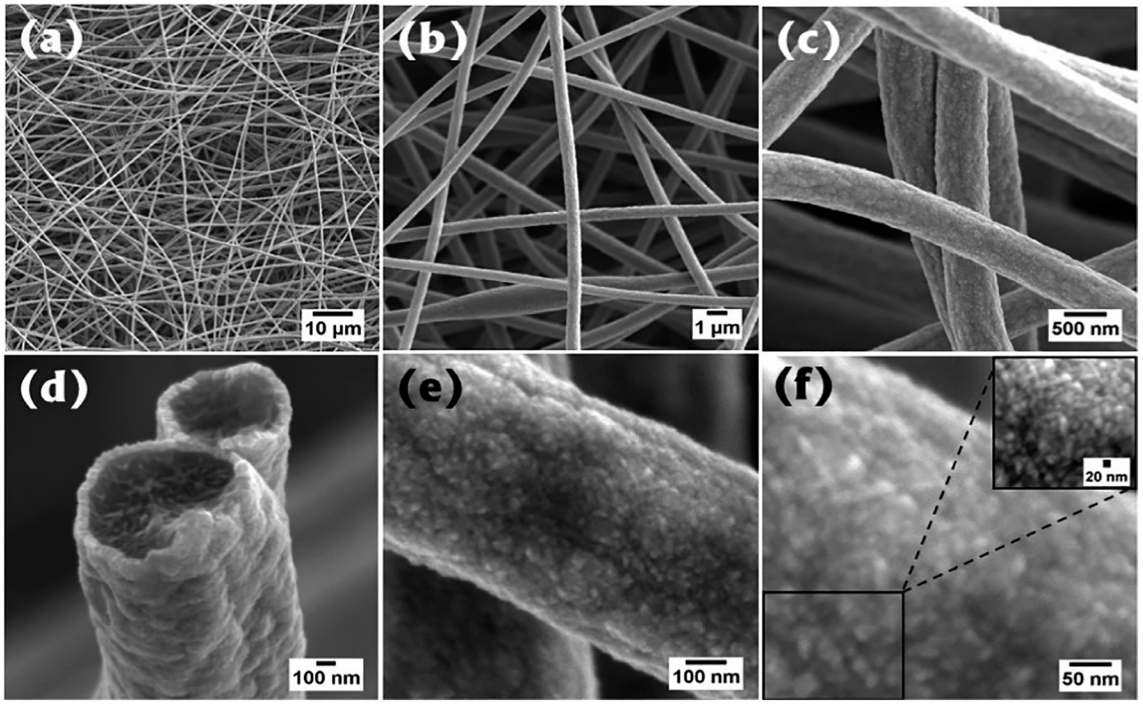

Fig. 2. SEM images of PAN/ZnO nanofibers: (a–c) PAN/$ZnO_{50\ nm}$ top-view with different magnifications; the core-shall structure of single nanofibers (thickness ~50 nm) (d); the crystalline structure of PAN/$ZnO_{20\ nm}$ nanofibers (e–f).

from 10 to 50 nm, the crystallinity of the structure is increasing, which allows to estimate the average size of ZnO nanocrystallites the Debye–Scherrer's equation [35].

$$D = \frac{0,\ 9 \bullet \lambda}{\beta \bullet \cos(\theta)}, \tag{1}$$

where β, θ, and λ are full width of half maximum, diffraction angle, and x-ray wavelength (λ = 0.154 nm), respectively. The calculated average size of ZnO nanocrystallites was about 9 ± 2 nm for all samples what in agreement with the TEM measurements.

Furthermore, EDX mapping of a single PAN/ZnO nanofiber (Fig. 4b) indicate the oxygen and zinc content and distribution on the ZnO shell, while the carbon content attributed the PAN fiber, remains at the fiber's core. Besides, this mapping confirms that Zn and O are homogeneously dispersed.

The PL spectra of PAN/ZnO nanofibers are shown in Fig. 5a. The narrow peak in the ultraviolet (UV) region (375 ± 5 nm) corresponds to the near band emission (NBE) [27,36]. This band can also be

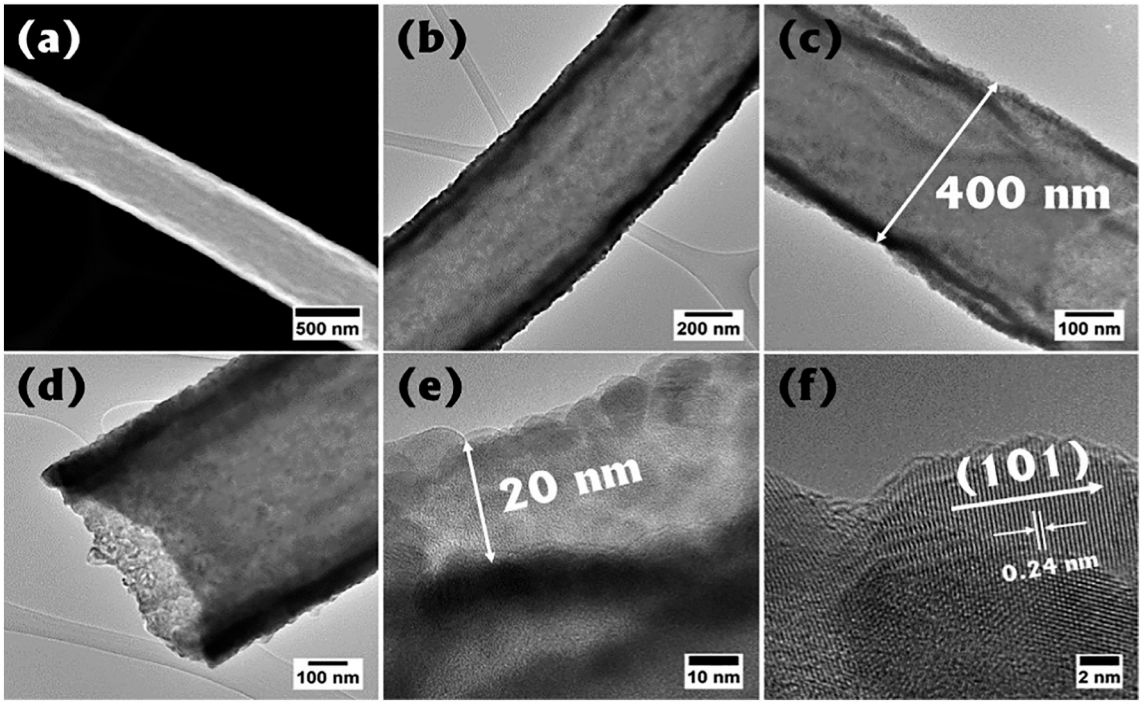

Fig. 3. TEM images of PAN/ZnO nanofibers: ZnO layer 20 nm (c, e, f); ZnO layer 50 nm (a, b, d).

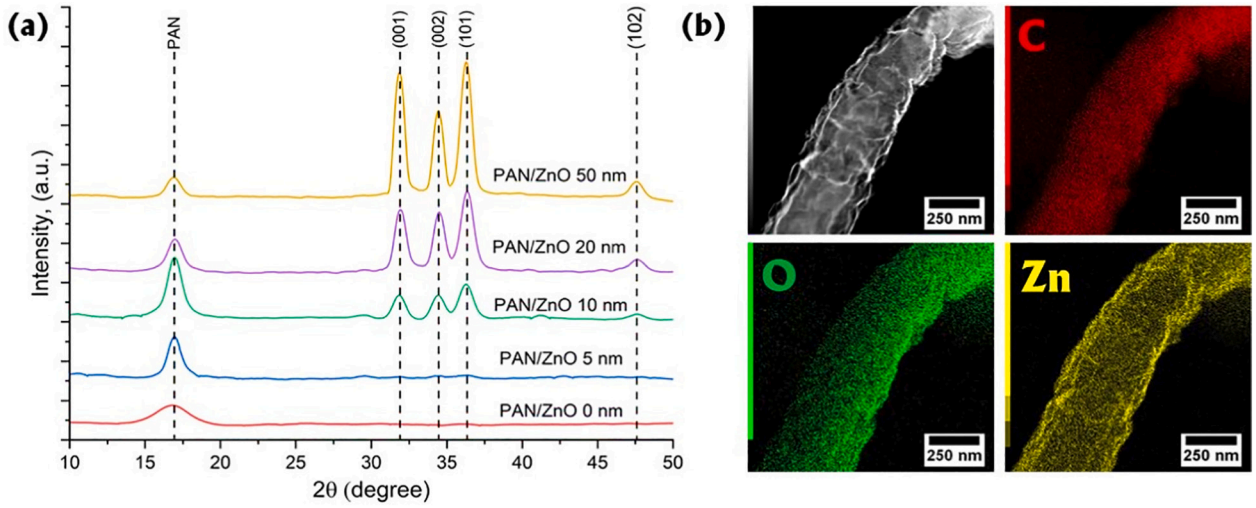

Fig. 4. XRD spectra of the obtained PAN/ZnO nanofibers (a) and EDX mapping of the single nanofiber with ZnO layer thickness 20 nm (b).

interpreted by the emission (3.34 eV) of free excitons (FE) in the bandgap of ZnO nanocrystallites [23]. The broad peak in the visible range around 565 nm corresponds to the deep defect levels (DLE) such as zinc vacancies (Zn_i^{++}), single (V_o^+) and double (V_o^{++}) ionized oxygen vacancies, neutral oxygen vacancies (V_o), and oxygen interstitials (O_i) [37]. The deconvolution of DLE emission (Fig. 5b) reveals three general types of defects involved in the green-blue PL process: V_o^+ (2,45 eV), V_o^{++} (2,23 eV), O_i (2 eV) (inset Fig. 5b) [36,38]. The peak around 785 nm attributes to the residual PL emission of PAN nanofibers. The decrease of PL in the visible region upon increasing the thickness of the ZnO layer can be explained by the improvement of the crystallinity of semiconductor and thus, the reduction of defect concentration [39]. However, the low UV emission and high DLE to NBE ratio indicate the high defects concentration within the ZnO structure [23,36].

Taking into account the findings from PL analysis, and to achieve a stable, reliable, and repeatable results for the developed PL biosensing platform, it was decided to use PAN/ZnO nanofibers with an oxide layer of 20 nm that is capable of providing the conformal coverage over the PAN, relatively high PL emission and the stable biorecognition layer.

3.2. The evaluation of PAN/ZnO PL-based immunosensor

3.2.1. Biofunctionalization

It is important for biosensors to detect selectively the target molecules while the remaining molecules must not affect the sensor's response. In order to achieve the selective adsorption of AFB1 to the PAN/ZnO surface, the bioselective (biorecognition) layer containing Anti-AFB1 was formed along the step-by-step biofunctionalization process (Fig. 6a). The blank PAN/ZnO_{20nm} nanofibers during the silanization (APTES treatment) process and GA activation were prepared for conjugation with the Anti-AFB1. The detailed biofunctionalization protocol was as follows: i) to achieve the thin APTES layer which acts as a coupling agent between the PAN/ZnO_{20nm} and Anti-AFB1, nanofibers were treated by 10 μl of 2% APTES solution in Ethanol (99.9%) at room temperature (RT) for 10 min. Then the sample was gently washed with Ethanol (99.9%) with the following drying on a hot plate at 85 °C for 1 h. ii) At the next step, PAN/ZnO_{20nm}/APTES samples were immersed in a 1% GA water solution (at RT for 1 h) to activate APTES modified surface. Subsequently, the PAN/ZnO/APTES/GA was rinsed with DI water to avoid non-specific adsorption of the Anti-AFB1. iii) The GA-activated surface was then reacted with 10 μl of 50 μg/ml Anti-AFB1 solution in PBS buffer (pH 7.4) at RT for 30 min to form a bioselective layer of anti-AFB1. Then, PAN/ZnO/APTES/GA/Anti-AFB1 was rinsed

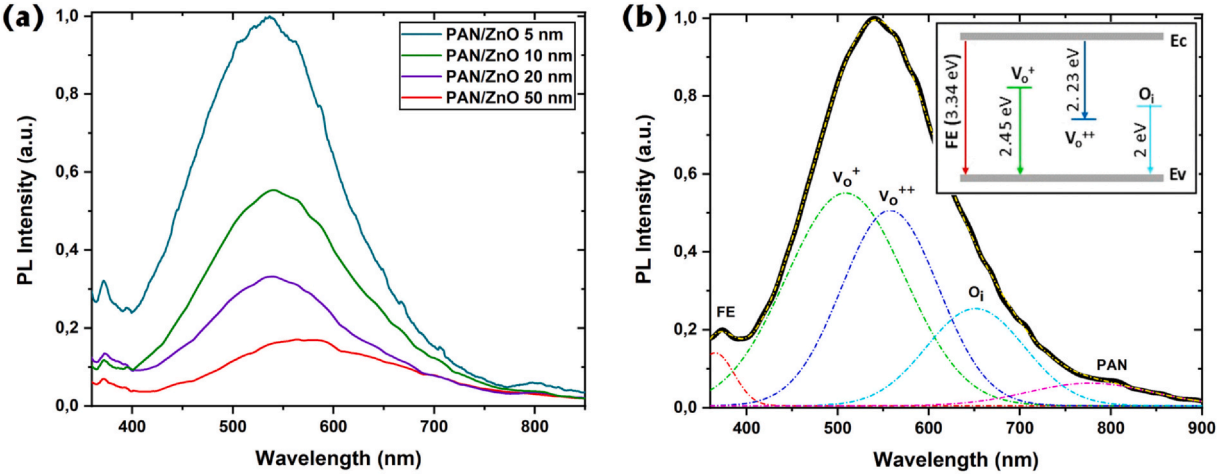

Fig. 5. PL spectra of PAN/ZnO nanofibers with different thicknesses of ZnO layer (a) and (b) PL deconvolution with Gaussian function; inset - possible optical transitions and their energies in ZnO nanostructures, where free excitons (FE), single ionized oxygen vacancies (V_o^+), double ionized oxygen vacancies (V_o^{++}), and oxygen interstitials (O_i).

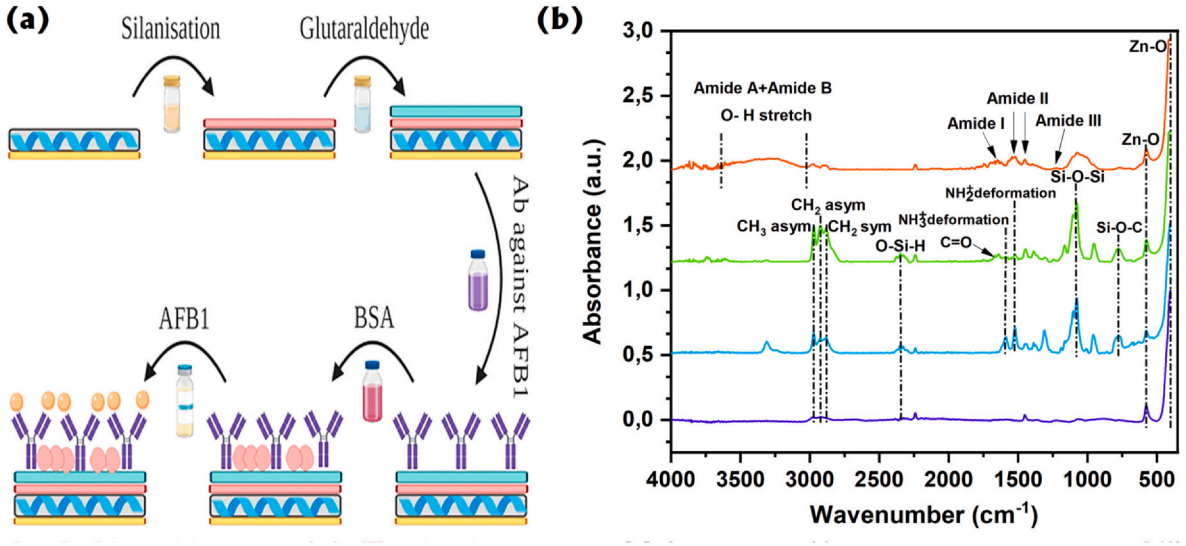

Fig. 6. Step by step biofunctionalization process (a) and (b) FTIR spectra of the following biofunctionalization stages: dark blue – bulk PAN/ZnO_{20nm} sample; bright blue line – PAN/$ZnO_{20\ nm}$/APTES; green – PAN/ZnO_{20nm}/APTES/GA; red line – PAN/ZnO_{20nm}/APTES/GA/Anti-AFB1. (For interpretation of the references to colour in this figure legend, the reader is referred to the web version of this article.)

with PBS to wash out non – conjugated antibodies. iv) 10 μl of 5 μg/ml of BSA was added to block the remaining active sites that enable adsorb proteins. v) As a result, PAN/ZnO_{20nm}/APTES/GA/Anti-AFB1 was formed.

To confirm the biofunctionalization of PAN/ZnO_{20nm} nanofibers by APTES, GA, and Anti-AFB1 a series of FTIR measurements were performed (Fig. 6b). The peak at 480 cm^{-1} is attributed to an electronic transition to deep surface states that originated from defects (oxygen vacancies) in the ZnO layer [40].The significant changes have appeared in the FTIR spectrum when the silanization process is done. Peaks from the Si-O-C (777 cm^{-1}), Si-O-Si (1078 cm^{-1}), NH_2 (1529 cm^{-1}), NH_3 (1596 cm^{-1}), O-Si-H (2341 cm^{-1}), and, CH_2 (2878–2931 cm^{-1}) and CH_3 (2977 cm^{-1}) groups indicate the formation of APTES layer. The GA-activation of APTES modified nanofibers results in appearing of peaks at 1635–1690 cm^{-1} which can be attributed to the C═O or/and C═C stretchings of GA molecule [41]. Afterward, Anti-AFB1 were added to form a layer selective to AFB1 molecules. The aldehyde groups on the surface react with amino groups of antibodies and proteins for covalent immobilization by an amide bond formation. The peaks in the range of 1226–1666 cm^{-1} can be associated with the amide I (1642–1660 cm^{-1}), amide II (1450–1535 cm^{-1}) and amide III (1226–1233 cm^{-1}) bonds. Additionally, one can assume that peaks in the range of 3005–3730 cm^{-1} correspond to the amide A and amide B bonds, on the other hand, such a broad peak can appear due to the O—H stretching.

3.2.2. Aflatoxin B1 PL detection

Quantitative analysis of the interactions between PAN/ZnO_{20nm}/APTES/GA/Anti-AFB1 structure and AFB1 molecules was performed in the concentration range of 0.1–100 ng/ml (target AFB1). To simplify the calculation of the main biosensors parameters (LOD, sensitivity range, etc.), PL signals of PAN/ZnO_{20nm} nanocomposite were normalized as follows:

$$I_{Cn} = \frac{I_C}{I_{Cmax}}, \tag{2}$$

where I_{Cn} is the normalized PL signal for each concentration as shown in the Fig. 7, I_C is the non-normalized PL signal for each AFB1 concentration, and I_{Cmax} – maximum PL signal (C_{AFB1} = 118.1 ng/ml).

Fig. 7a shows that the PL signal increases while the AFB1 molecules bind to the PAN/ZnO_{20nm}/APTES/GA/Anti-AFB1 surface. One may observe the 25% increasing of the PL intensity for the concentration of AFB1 around 100 ng/ml. The saturation of the analytical PL signal is observed in the range of 20–100 ng/ml what imposes an upper limit for the AFB1 detection (Fig. 7a). The saturation can be explained considering that the great majority of antibodies (anti-AFB1) are bonded to the AFB1 molecules. Besides, no significant changes in the PL were identified for control samples. Fig. 7b shows the sensor signal (response curve) of PAN/ZnO_{20nm}/APTES/GA/Anti-AFB1 structure vs the concentration of AFB1. The linear fitting (dark blue line) of the experimental data (bright blue spots) can be expressed by the formula:

$$I_{PL565,2} = 0.489 - 0.385 \cdot Log(C), \tag{3}$$

where C is the AFB1 concentration.

Considering the Eq. (3), the LOD was calculated using the formula:

$$LOD = 3.3 \bullet \sqrt{n} \bullet \frac{\sigma}{b}, \tag{4}$$

where σ is the standard deviation of the negative control at small concentrations, n – number of tests, b is the slope of the curve, extracted from Eq. (3). The calculated value of LOD was around 39 ± 1 pg/ml, which is significantly lower than the acceptable levels of AFB1 in human foods and beverages (European Commission, No 401/2006). The calculated LOD value for PAN/ZnO PL-based biosensor is comparable with results obtained elsewhere [15,42,43] or even lower than that reported by Alshannaq et al. and Moon et al. [44,45]. This result shows that the studied nanostructures and the detection approach could be further applied for the development of efficient immunosensors and novel biosensors with other types of biorecognition agents (e.g. enzymes, DNA). A comparison of typical optical (label-free) biosensors for AFB1 detection is presented in the Table 1, in which the LOD of current immunosensor is at a low level, with the sensitivity range similar to the others.

3.2.3. The mechanism of PL biosensing

To gain further insights regarding the mechanisms of PL detection, we decided to develop a model that could explain the PL changes in semiconductors during the adsorption of molecules. According to the theory of PL in semiconductors, the changes of PL signal can be associated with the bandgap modification (e.g. band bending) under additional external forces that could be caused by the adsorption of the proteins which will affect the surface band bending. Those forces mostly initiate the surface potential ψ_s changes resulting in expanding or constriction of the space charge region (SCR) and/or energy band

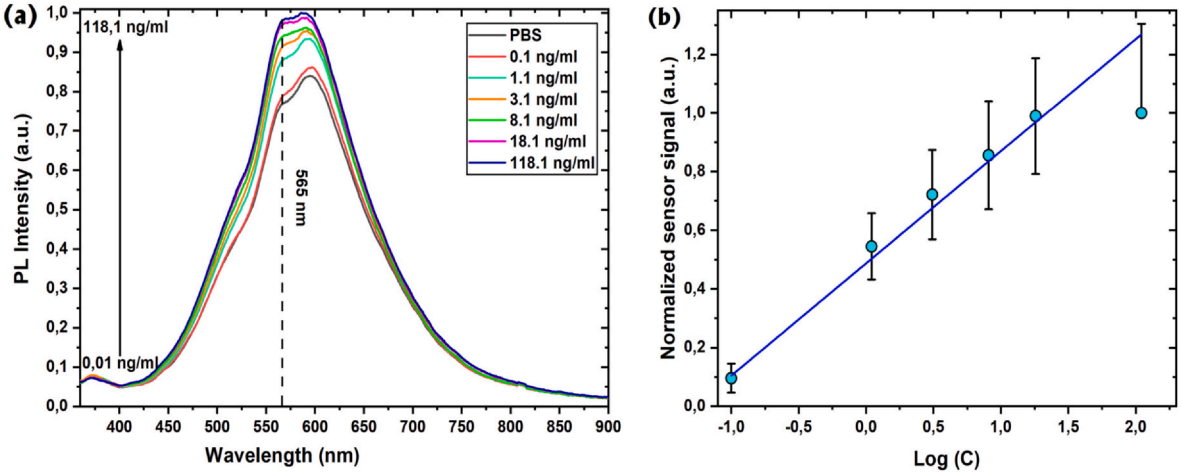

Fig. 7. Photoluminescence spectra of PAN/ZnO_{20nm}/APTES/GA/Anti-AFB1 biosensor after incubation in different AFB1 concentrations (from bottom to top) containing samples after the reaching of steady state conditions; (b) the response curve, measured at PL peak position (λ = 565 nm).

bending. The existence of a surface potential barrier that needs to be overcome by the photogenerated carriers and the value of SCR strongly affects the recombination processes, and as a consequence, the PL in semiconductors.

Being in liquids/electrolytes, semiconductor experience a significant influence of ions and the surface potential ψ_s depends on the total charge of all ions at the defined distance from the surface (Debye length) [54]. Besides, if the liquid contains macromolecules, such as proteins (antibodies, antigens, etc.), they will induce an additional effect on φ_D. It means that the PL signal is defined by the ψ_s, which is determined by the total electrostatic potential of both ions in the liquid and protein charges near the semiconductor surface.

There are two hypotheses of the electrostatic influence of protein charges which penetrate the diffuse layer (Helmholtz layer) to the semiconductor interface [55]. The first hypothesis is based on the Debye model, which defines the thickness of diffuse-charged layers by the distance (Debye length) where the electrostatic field has dropped to $1/e$ of its initial value. However, the Debye length in a physiological salt solution is limited to be around 0.8 nm [55]. It means only that the charge density changes comparable to the value of a Debye length can be detected. As we deal with proteins, such as antibodies and antigens, with an average size ($> 10\ nm$) much bigger than the Debye length, one may conclude that their charges will be "not seen" for the detection platform [55].

The second hypothesis can be described by the so-called Donnan model [56]. This model enables to consider the influence of charge density changes caused by antibodies and antigens at the distances comparable to the Debye length. The main idea of this model based on the assumption that there are two phases (s and m) at the interface semiconductor/electrolyte, in which ions can freely diffuse to the surface until the electrostatic equilibrium state is achieved. Phases m and s represent the protein layer on the semiconductor surface and the volume of the electrolyte, respectively. The total electrostatic potential of the surface φ_D caused by ions and proteins in the Helmholtz layer (phase m) can be described by the equation [57]:

$$\varphi_D = \frac{RT}{F} \ln\left(\frac{C_{p+} + \sqrt{4C_s^2 + C_{p+}^2}}{2C_s}\right), \tag{5}$$

where R, T, F are the universal gas constant, temperature, and Faraday constant respectively, while C_{p+} and C_s are the concentration of protein-fixed positive charges and the ion concentrations in phase m [55]. As seen from the Eq. (5), the Donnan potential (potential arises between two phases) mostly depends on the ion equilibrium concentrations in phase m. It worth to mention that there is a smooth transition between the φ_D and the surface potential (ψ_s) of semiconductor [58], which means that the changes of φ_D caused by ions transfer between m and s phases will influence on the surface potential $\psi_s(\varphi_D)$. Taking into account that the value of SCR is proportional to the square root of ψ_s, it becomes obvious that the changes of φ_D will affect the SCR as well [59].

One may consider two different cases: *(i)* the surface potential of $\psi_{s1}(\varphi_{D1})$ for the surface functionalized by antibodies, and *(ii)* the surface potential of $\psi_{s2}(\varphi_{D2})$ for the surface with antibody-antigen complexes. While the n-type semiconductor (e.g. ZnO) possesses the positive ψ_s (bending up), the binding of the positively-charged proteins (e.g. AFB1) induces a downward band-bending and decreasing of ψ_s ($\psi_{s1}(\varphi_{D1}) > \psi_{s2}(\varphi_{D2})$) due to the ion concentrations change in the phase m [60]. Such antibody-antigen interaction will promote decreasing of the semiconductor ψ_s and the value of SCR. This will promote an increase of charge carrier concentration and, as a consequence, it will enhance the radiative recombination from the bulk defect states.

Based on this analysis, one may present the mechanism of PL changes in PAN/ZnO nanostructures after the adsorption of ABF1 molecules. Taking into account that we deal with the n-type semiconductor

Table 1
Representative results of recent label-free optical biosensors for AFB1 detection.

Biosensor performance	Transducer	Sensitivity range	LOD	Reference
Polarized optical microscopy	Liquid crystal	0.1–1 ng/ml	0.1 ng/ml	[46]
Fluorescence	g-C_3N_4 + Fe_3O_4	0.01–0.5ng/ml	0.002ng/ml	[47]
Fluorescence	TPE-Z + GO	–	0.25 ng/mL	[48]
Fluorescence	MIP-membrane	14–500 ng/ml	14 ng/ml	[49]
Plasmonic ELISA	AuNRs	0.0031–0,15 ng/ml	0.0125 ng/ml	[50]
Localized SPR	AuNPs	1–10 ng/ml	0.36 ng/ml	[51]
Colorimetric	G-quadruplex signal reporter	1 pM-100 nM	1pM	[52]
Electrochemiluminescence	Printed bipolar electrode	0.1–100 ng/ml	0.033 ng/ml	[53]
Photoluminescence	PAN/ZnO	0.1–20 ng/ml	0.039 ng/ml	This work

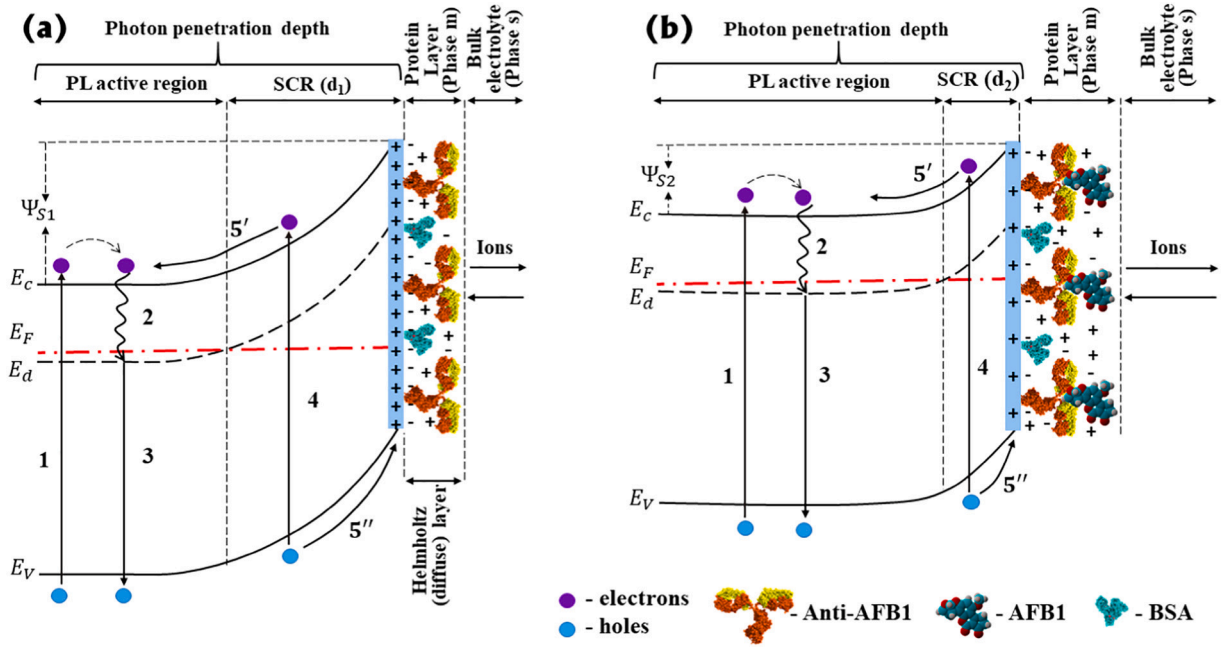

Fig. 8. Sketch of the energy band diagram of the ZnO nanolayer with two types of surface modifications: PAN/ZnO_{20nm}/APTES/GA/Anti-AFB1/BSA (a) and PAN/ZnO_{20nm}/APTES/GA/Anti-AFB1/BSA&AFB1 (b). The transition **1** is the excitation of the electron-hole pair under UV light irradiation, **2** – non-radiative transition of the electron to the defect level, **3** is the radiative transition, which is the PL in the visible region, **4** – non-radiative transition in the space charge region (SCR), **5′** indicates the electron migration from the surface to the volume of ZnO, **5″** indicates the holes migration from volume to the ZnO interface.

and positively charged AFB1 molecules [61], the bandgap diagrams of PAN/ZnO_{20nm}/APTES/GA/Anti-AFB1 in PBS solution before and after the adsorption of AFB1 molecules are shown in Fig. 8a and b, respectively. Let us assume that only one type of defects (see Fig. 8, E_d level) in ZnO defines the radiative recombination and the PL intensity. However, the radiative recombination of photogenerated holes and electrons will take place only when the defect level energy lies below the Fermi level (E_F) of ZnO. This condition will only be met for the bulk region called here the PL active region (Fig. 8). It is clearly seen that the width of the PL active region is modulated by the value of SCR and the ψ_s, which values strongly depend on the concentration of adsorbed AFB1 molecules and the ion concentrations in the Helmholtz layer.

Fig. 8a shows the upward band bending with the surface potential $\psi_{s1}(\varphi_{D1})$ and the SCR (d_1), for PAN/ZnO_{20nm}/APTES/GA/Anti-AFB1. The PL intensity is determined by radiative transitions 1 → 2 → 3 (Fig. 8). The expanding of SCR (increasing of ψ_s) will subsequently lead to the constriction of the PL active region and it will decrease the probability of radiative transitions 1 → 2 → 3. On the other hand, the reducing of SCR will have an opposite effect and, as a result, increasing PL intensity. After positively charged AFB1 molecules interact with antibodies (Anti-AFB1), it should downward the band bending (Fig. 8b). This downward band bending is associated with the lower value of ZnO surface potential $\psi_{s2}(\varphi_{D2})$ and it promotes constriction of the SCR to the value d_2. Thus, the probability of radiative transitions 1 → 2 → 3 in the PL active region increases, while the probability of non-radiative transitions (transition 4) and the charge carriers separation (transition 5′-5″) becomes lower. This condition promotes increasing of PL intensity for PAN/ZnO_{20nm}/APTES/GA/Anti-AFB1/BSA &AFB1 nanostructures after the adsorption of positively charged AFB1 molecules on the surface.

The proposed mechanism of optical biosensing is based mostly on the photoluminescence studies and the theory of semiconductor surfaces. In order to prove the reliability of the proposed mechanism to other types of biosensors (e.g. FET biosensors), more specific techniques should be applied, such as Electrochemical Impedance Spectroscopy (EIS), EIS microscopy, THz spectroscopy etc.

3.2.4. *Kinetic and thermodynamic aspects*

Kinetic and thermodynamic analysis may provide important information on biomolecular interactions between antibody and antigen. Moreover, kinetic analysis offers insights concerning the relationships between structure and biochemical activities. The basis of kinetic and thermodynamic analysis is adsorption isotherm interpretation, which allows calculating some important biosensor parameters, such as adsorption affinity constant, Gibbs free energy change, and power coefficient. Fig. 9a presents the time-resolved PL intensity changes of the PAN/ZnO_{20nm}/APTES/GA/Anti-AFB1 sample vs different AFB1 concentrations. The immunosensor response time to the different AFB1 concentrations was in the range of 15–20 min. The dashed lines indicate the steady-state conditions for each concentration. The total AFB1 concentration interacted with the PAN/ZnO_{20nm}/APTES/GA/Anti-AFB1 surface was calculated as the sum of all infused concentrations during the test. Biosensor responses vs various ABF1 concentrations (Fig. 9b) were calculated using the formula [15]:

$$S(C) = I_{eq}(C) - 1, \tag{6}$$

where I_{eq} and C are the normalized PL signal value of the PAN/ZnO_{20nm}/APTES/GA/Anti-AFB1 sample in steady state conditions and the value of AFB1 concentration, respectively.

Adsorption isotherm indicates a pseudo-first-order interaction between AFB1 and PAN/ZnO_{20nm}/APTES/GA/Anti-AFB1 structure as shown in Fig. 9b. This type of interaction can be described by the first order kinetic equation (Langmuir equation) obtained from the fitting (dark blue curve) [62]:

$$\frac{dN}{dt} = k_a \cdot C \cdot (N_s - N) - k_d \cdot N, \tag{7}$$

where N, k_a, k_d, N_s and C are a number of adsorbed molecules, an association constant, a dissociation constant, a number of adsorption sites and the concentration, respectively.

In this particular case, the number of adsorbed molecules has maximum value, while the sensitivity is highest. It means that those parameters are proportional $N_s \sim S_{max}$, and N is proportional to the biosensor sensitivity ($N \sim S$, where $S < S_{max}$).

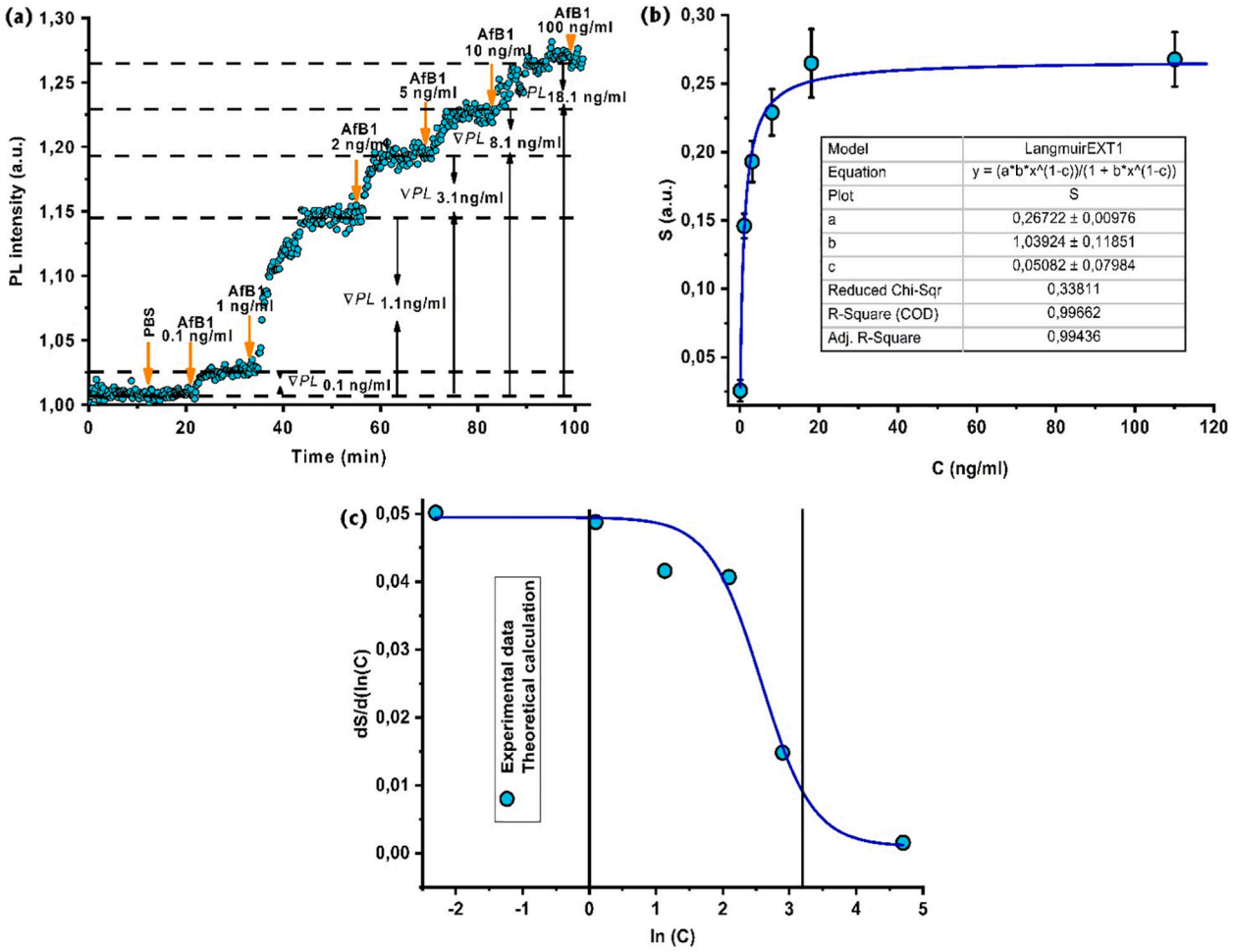

Fig. 9. Dependence of PL peak maximum (at λ = 565 nm) vs AFB1 concentration; (b) the isotherm of analyte (AFB1) interaction with PAN/ZnO_{20nm}/APTES/GA/Anti-AFB1 structure; and (c) calculated sensitivity of PAN/ZnO_{20nm}/APTES/GA/Anti-AFB1 structure towards AFB1.

It should be noted, that after adding of AFB1 into the microfluidic cell, the PL intensity increases until its saturation, which indicates the steady-state conditions between PAN/ZnO_{20nm}/APTES/GA/Anti-AFB1 and AFB1. Thus, the rate of AFB1 adsorption is equal to zero $\left(\frac{dN}{dt} = 0\right)$, and the Eq. (7) can be rewritten as follows:

$$k_a \cdot C \cdot (S_{max} - S) - k_d \cdot S = 0. \quad (8)$$

After some additional calculations, the Langmuir Eq. (8) is transformed to the Eq. (9), while fitting parameters are taken from the Eq. (10) (inset, Fig. 9b):

$$\frac{S}{S_{max}} = \frac{K_A \bullet C}{1 + K_A \cdot C}, \quad (9)$$

$$\frac{y}{a} = \frac{b \cdot x^n}{1 + b \cdot x^n}, \quad (10)$$

where $b = K_A = \frac{k_a}{k_d}$, is the affinity constant, $x = C$ – concentration, $n = 1 - c$ is the power coefficient (*c*-fitting parameter from the inset table of Fig. 9b), *y*, *a* are *S* and S_{max} respectively.

The affinity dissociation constant $K_D = 0.96 \pm 0.11$ *ng/ml* was calculated as the reversed value of K_A and allows one to estimate the change in Gibbs free energy (ΔG) of PAN/ZnO_{20nm}/APTES/GA/Anti-AFB1 & AFB1 complex formation:

$$\Delta G = RT \bullet Ln\ K_D^0, \quad (11)$$

where *R* and *T* are the universal gas constant and the absolute temperature, respectively. The value $K_D{}^0 = K_D/C$, in this case, *C* is the standard reference concentration of 1 M.

The obtained value of the change in Gibbs free energy $\Delta G = -44.6 \pm 1.4$ *kJ/mol* indicates the thermodynamically favorable reaction of the chemical adsorption [63] for the PAN/ZnO_{20nm}/APTES/GA/Anti-AFB1&AFB1 complex formation [64]. One can conclude that a strong electrostatic chemical bonding occurs between the PAN/ZnO_{20nm}/APTES/GA/Anti-AFB1 and AFB1 molecules. The calculated ΔG is in good agreement with the value obtained in our previous research [15] and higher than recently reported for the AFB1 physisorbed onto the detection platform [65].

The calculated power coefficient $n = 0.95 \pm 0.01$ indicates a favorable sorption process ($n < 1$) of the analyte onto the PAN/ZnO_{20nm}/APTES/GA/Anti-AFB1 structure [66] and the fast diffusion of AFB1 molecules to the developed nanofibers structure [17]. Besides, such value of the power coefficient ($0.5 < n < 1$) can be additionally explained by the partially negative cooperative adsorption [67]. The negative cooperative adsorption indicates the decreasing of affinity while the molecule covalently binds with the binding site. Taking into account that the structure of antibodies assumed to be bivalent [68], because of V regions of the two heavy and light chains, it offers two identical antigen-binding sites [69]. Therefore, it can be supposed that binding affinity (capability) of Anti-AFB1 towards AFB1 becomes lower after the first Anti-AFB1&AFB1 binding and tends to the zero value after the second Anti-AFB1&AFB1 binding.

Finally, the sensitivity of PAN/ZnO_{20nm}/APTES/GA/Anti-AFB1 was calculated as the derivative of the sensor signal response *S* to the natural logarithm of AFB1 concentration *C* (Fig. 10c). Analysis of the

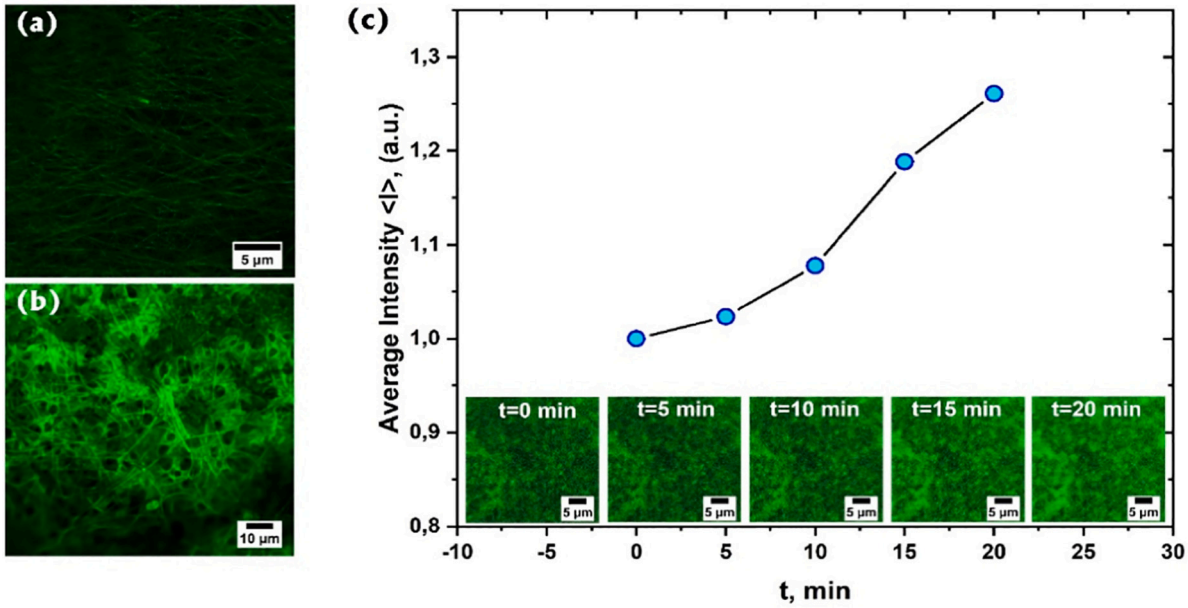

Fig. 10. The images obtained via fluorescent confocal microcopy: (a) bulk PAN/ZnO_{20nm} nanofibers (b) and PAN/ZnO_{20nm}/APTES/GA/Anti-AFB1 structures. (c) the time-resolved PL intensity of PAN/ZnO_{20nm}/APTES/GA/Anti-AFB1, concentration of AFB1–10 ng/ml.

sensitivity indicates, that the PAN/ZnO_{20nm}/APTES/GA/Anti-AFB1 biosensor shows the sensitivity towards AFB1 molecules in the range of 0.1–20 ng/ml. However, the upper limit can achieve higher values than 20 ng/ml of AFB1 concentration, if more Anti-AFB1 would be immobilized on the PAN/ZnO_{20nm}/APTES/GA structure.

All analytical parameters and kinetic constants of the PAN/ZnO_{20nm}/APTES/GA/Anti-AFB1&AFB1 complex are presented in Table 2.

3.2.5. *Microscopy visualization*

In the final stage of the research, the two-photon PL microscopy was used to visualize immunosensor response during PAN/ZnO_{20nm}/APTES/GA/Anti-AFB1&AFB1 complex formation. Fig. 10(a, b) demonstrate the PL emission from PAN/ZnO_{20nm} and PAN/ZnO_{20nm}/APTES/GA/Anti-AFB1, respectively. It is clearly seen the more intense PL emission for the sample with immobilized antibodies that proves the mechanism provided in Section 3.2.2. This means that after immobilization of Anti-AFB1 to the surface of the PAN/ZnO_{20nm} sample, the downward band-bending and decreasing of ψ_s lead to increasing of PL intensity. Besides, the uniform PL emission from PAN/ZnO_{20nm}/APTES/GA/Anti-AFB1 nanofibers proves the conformal functionalization of the ZnO surface. Then, the probe of AFB1 with a concentration of 10 ng/ml was injected into the cell with the PAN/ZnO_{20nm}/APTES/GA/Anti-AFB1 and the control sample. The PL images/frames have been recorded every 5 min until signal saturation. Fig. 10c shows the time-dependent average intensity of PL for the PAN/ZnO_{20nm}/APTES/GA/Anti-AFB1&AFB1. It is seen that the PL intensity progressively increases over time. The PL images were analyzed using ImageJ software. The inset image indicates the change in average PL intensity during the APTES/GA/Anti-AFB1&AFB1 complex formation. The average PL intensity was about (~ 26%), and has a good agreement with the value (~ 25%) from PL-based real-time measurement for AFB1 10 ng/ml concentration (Fig. 9b). A control experiment was also conducted on the PAN/ZnO_{20nm} sample. No significant non-specific adsorption of AFB1 was observed. The results confirm that the produced immunosensor provides a sensing capability with a high signal-to-noise ratio and diminished non-specific adsorption.

4. Conclusions

In conclusion, PAN/ZnO nanofibers prepared by electrospinning and ALD was successfully examined as a PL-based platform for AFB1 detection. The intensity of the PL emission of PAN/ZnO_{20nm} modified by APTES/GA/Anti-AFB1 is seen to be dependent on the AFB1 concentration, evidencing an increase of PL with increasing concentration of the analyte. PAN/ZnO_{20nm}/APTES/GA/Anti-AFB1 samples were integrated into the microfluidic cell, which showed high sensitivity towards AFB1 molecules in the range of 0.1–20 ng/ml, and the LOD was evaluated as 39 pg/ml. The immunosensor response time to the different AFB1 concentrations was in the range of 15–20 min. The calculated values of kinetic constants and thermodynamic parameters indicate favorable AFB1 adsorption to the PAN/ZnO_{20nm}/APTES/GA/Anti-AFB1 immunosensor as well as high electrochemical interaction between immunosensor and AFB1 due to the Anti-AFB1&AFB1 complex formation. The results obtained by the two-photon PL microscopy confirm that the developed immunosensor is capable to detect AFB1 with a high signal-to-noise ratio and diminished non-specific adsorption. Besides, the model of semiconductor – analyte interaction and its effect on PL emission was proposed and analyzed. The obtained results indicate the suitability of our materials and detection approach to be employed in the fabrication of biosensing devices for probing other relevant analytes. In the future researches, it is planned to develop the immunosensor prototype based on ZnO nanofibers and on this detection approach (PL detection scheme) towards different types of mycotoxins presented in the products.

Table 2
Calculated parameters of real – time AFB1 detection and adsorption.

LOD, pg/ml	***S***, ng/ml	***n***	K_D, ng/ml	K_D, M	ΔG, kJ/mol
39 ± 1	0.1–20	0.95 ± 0.01	0.96 ± 0.11	$29.5 \cdot 10^{-10} \pm 2.2 \cdot 10^{-11}$	−44.6 ± 1.2

CRediT authorship contribution statement

Conceptualization, I.I.; methodology, I.I.; sample fabrication, M.B.; XRD, TEM investigations, E.C.; optical and biosensing investigations, V.M., I.I.; writing—original draft preparation, V.M.; writing—review and editing, I.I., M.B, E.C; supervision, I.I.; project administration, I.I.; funding acquisition, I.I.

Declaration of competing interest

The authors declare that they have no known competing financial interests or personal relationships that could have appeared to influence the work reported in this paper.

Acknowledgments

I.I., E.C., V.M., and M.B. acknowledge the financial support by project H2020-MSCA-RISE-2017, 'Novel 1D photonic metal oxide nanostructures for early stage cancer detection' (Project number: 778157). V.M. acknowledge the partial financial support from the project "Środowiskowe interdyscyplinarne studia doktoranckie w zakresie nanotechnologii" No. POWR.03.02.00-00-I032/16 under the European Social Fund – Operational Programme Knowledge Education Development, Axis III Higher Education for Economy and Development, Action 3.2 PhD Programme.

References

[1] R. Chauhan, J. Singh, T. Sachdev, T. Basu, B.D. Malhotra, Recent advances in mycotoxins detection, Biosens. Bioelectron. 81 (2016) 532–545, https://doi.org/10.1016/j.bios.2016.03.004.
[2] D.J. Miller, Fungi and mycotoxins in grains: implication for stored roducts research, J. Stored Prod. Res. 31 (1995) 1–16.
[3] L. Rieswijk, S.M.H. Claessen, O. Bekers, M. van Herwijnen, D.H.J. Theunissen, D.G.J. Jennen, T.M.C.M. de Kok, J.C.S. Kleinjans, S.G.J. van Breda, Aflatoxin B1 induces persistent epigenomic effects in primary human hepatocytes associated with hepatocellular carcinoma, Toxicology. 350–352 (2016) 31–39, https://doi.org/10.1016/j.tox.2016.05.002.
[4] S. Marchese, A. Polo, A. Ariano, S. Velotto, S. Costantini, L. Severino, Aflatoxin B1 and M1: biological properties and their involvement in cancer development, Toxins (Basel) 10 (2018) 214, https://doi.org/10.3390/toxins10060214.
[5] M.J. Adegbeye, P.R.K. Reddy, C.A. Chilaka, O.B. Balogun, M.M.M.Y. Elghandour, R.R. Rivas-Caceres, A.Z.M. Salem, Mycotoxin toxicity and residue in animal products: prevalence, consumer exposure and reduction strategies – a review, Toxicon. 177 (2020) 96–108, https://doi.org/10.1016/j.toxicon.2020.01.007.
[6] P. Battilani, P. Toscano, H.J. Van Der Fels-Klerx, A. Moretti, M. Camardo Leggieri, C. Brera, A. Rortais, T. Goumperis, T. Robinson, Aflatoxin B 1 contamination in maize in Europe increases due to climate change, Sci. Rep. 6 (2016) 1–7, https://doi.org/10.1038/srep24328.
[7] Q. Xu, W. Shi, P. Lv, W. Meng, G. Mao, C. Gong, Y. Chen, Y. Wei, X. He, J. Zhao, H. Han, M. Sun, K. Xiao, Critical role of caveolin-1 in aflatoxin B1-induced hepatotoxicity via the regulation of oxidation and autophagy, Cell Death Dis. 11 (2020) 6, https://doi.org/10.1038/s41419-019-2197-6.
[8] N.A. Lee, S. Wang, R.D. Allan, I.R. Kennedy, A rapid aflatoxin B1 ELISA: development and validation with reduced matrix effects for peanuts, corn, pistachio, and soybeans, J. Agric. Food Chem. 52 (2004) 2746–2755, https://doi.org/10.1021/jf0354038.
[9] N.H.S. Ammida, L. Micheli, S. Piermarini, D. Moscone, G. Palleschi, Detection of Aflatoxin B 1 in Barley: comparative study of immunosensor and HPLC, Anal. Lett. 39 (2006) 1559–1572, https://doi.org/10.1080/00032710600713248.
[10] M. Puiu, L.G. Zamfir, V. Buiculescu, A. Baracu, C. Mitrea, C. Bala, Significance testing and multivariate analysis of datasets from surface plasmon resonance and surface acoustic wave biosensors: prediction and assay validation for surface binding of large analytes, Sensors (Switzerland). 18 (2018) 1–15, https://doi.org/10.3390/s18103541.
[11] D. Pan, G. Li, H. Hu, H. Xue, M. Zhang, M. Zhu, X. Gong, Y. Zhang, Y. Wan, Y. Shen, Direct immunoassay for facile and sensitive detection of small molecule aflatoxin B 1 based on nanobody, Chem. A Eur. J. 24 (2018) 9869–9876, https://doi.org/10.1002/chem.201801202.
[12] V. Myndrul, I. Iatsunskyi, Nanosilicon-based composites for (bio)sensing applications: current status, advantages, and perspectives, Materials (Basel). 12 (2019) 2880, https://doi.org/10.3390/ma12182880.
[13] D. Han, D. Ni, Q. Zhou, J. Ji, Y. Lv, Y. Shen, S. Liu, Y. Zhang, Harnessing photoluminescent properties of carbon nitride nanosheets in a hierarchical matrix, Adv. Funct. Mater. 29 (2019) 1905576, https://doi.org/10.1002/adfm.201905576.
[14] V. Myndrul, R. Viter, M. Savchuk, N. Shpyrka, D. Erts, D. Jevdokimovs, V. Silamiķelis, V. Smyntyna, A. Ramanavicius, I. Iatsunskyi, Porous silicon based photoluminescence immunosensor for rapid and highly-sensitive detection of Ochratoxin A, Biosens. Bioelectron. 102 (2018) 661–667, https://doi.org/10.1016/j.bios.2017.11.048.
[15] V. Myndrul, R. Viter, M. Savchuk, M. Koval, N. Starodub, V. Silamiķelis, V. Smyntyna, A. Ramanavicius, I. Iatsunskyi, Gold coated porous silicon nanocomposite as a substrate for photoluminescence-based immunosensor suitable for the determination of Aflatoxin B1, Talanta. 175 (2017) 297–304, https://doi.org/10.1016/j.talanta.2017.07.054.
[16] A. Tereshchenko, V. Fedorenko, V. Smyntyna, I. Konup, A. Konup, M. Eriksson, R. Yakimova, A. Ramanavicius, S. Balme, M. Bechelany, ZnO films formed by atomic layer deposition as an optical biosensor platform for the detection of Grapevine virus A-type proteins, Biosens. Bioelectron. 92 (2017) 763–769, https://doi.org/10.1016/j.bios.2016.09.071.
[17] R. Viter, M. Savchuk, I. Iatsunskyi, Z. Pietralik, N. Starodub, N. Shpyrka, A. Ramanaviciene, A. Ramanavicius, Analytical, thermodynamical and kinetic characteristics of photoluminescence immunosensor for the determination of Ochratoxin A, Biosens. Bioelectron. 99 (2018) 237–243, https://doi.org/10.1016/j.bios.2017.07.056.
[18] S. Hariharan, B. Karthikeyan, Band bending effect induced non-enzymatic highly sensitive glucose sensing in ZnO nanoparticles, J. Lumin. 183 (2017) 1–6, https://doi.org/10.1016/j.jlumin.2016.10.046.
[19] J. Politi, I. Rea, P. Dardano, L. De Stefano, M. Gioffrè, Versatile synthesis of ZnO nanowires for quantitative optical sensing of molecular biorecognition, Sensors Actuators B Chem. 220 (2015) 705–711, https://doi.org/10.1016/j.snb.2015.05.135.
[20] A. Tamashevski, Y. Harmaza, R. Viter, D. Jevdokimovs, R. Poplausks, E. Slobozhanina, L. Mikoliunaite, D. Erts, A. Ramanaviciene, A. Ramanavicius, Zinc oxide nanorod based immunosensing platform for the determination of human leukemic cells, Talanta. 200 (2019) 378–386, https://doi.org/10.1016/j.talanta.2019.03.064.
[21] A. Tereshchenko, M. Bechelany, R. Viter, V. Khranovskyy, V. Smyntyna, N. Starodub, R. Yakimova, Optical biosensors based on ZnO nanostructures: advantages and perspectives. a review, Sensors Actuators B Chem. 229 (2016) 664–677, https://doi.org/10.1016/j.snb.2016.01.099.
[22] Y. Zhang, M.K. Ram, E.K. Stefanakos, D.Y. Goswami, Synthesis, characterization, and applications of ZnO nanowires, J. Nanomater. 2012 (2012) 1–22, https://doi.org/10.1155/2012/624520.
[23] R. Viter, V. Khranovskyy, N. Starodub, Y. Ogorodniichuk, S. Gevelyuk, Z. Gertnere, N. Poletaev, R. Yakimova, D. Erts, V. Smyntyna, A. Ubelis, Application of room temperature photoluminescence from ZnO nanorods for Salmonella detection, IEEE Sensors J. 14 (2014) 2028–2034, https://doi.org/10.1109/JSEN.2014.2309277.
[24] F. Liu, M.M.K. Wong, S.K. Chiu, H. Lin, J.C. Ho, S.W. Pang, Effects of nanoparticle size and cell type on high sensitivity cell detection using a localized surface plasmon resonance biosensor, Biosens. Bioelectron. 55 (2014) 141–148, https://doi.org/10.1016/j.bios.2013.11.075.
[25] C.H. Sang, S.J. Chou, F.M. Pan, J.T. Sheu, Fluorescence enhancement and multiple protein detection in ZnO nanostructure microfluidic devices, Biosens. Bioelectron. 75 (2016) 285–292, https://doi.org/10.1016/j.bios.2015.08.050.
[26] I. Iatsunskyi, A. Vasylenko, R. Viter, M. Kempiński, G. Nowaczyk, S. Jurga, M. Bechelany, Tailoring of the electronic properties of ZnO-polyacrylonitrile nanofibers: experiment and theory, Appl. Surf. Sci. 411 (2017) 494–501, https://doi.org/10.1016/j.apsusc.2017.03.111.
[27] R. Viter, A. Abou Chaaya, I. Iatsunskyi, G. Nowaczyk, K. Kovalevskis, D. Erts, P. Miele, V. Smyntyna, M. Bechelany, Tuning of ZnO 1D nanostructures by atomic layer deposition and electrospinning for optical gas sensor applications, Nanotechnology. 26 (2015) 105501, https://doi.org/10.1088/0957-4484/26/10/105501.
[28] A. Barhoum, K. Pal, H. Rahier, H. Uludag, I.S. Kim, M. Bechelany, Nanofibers as new-generation materials: from spinning and nano-spinning fabrication techniques to emerging applications, Appl. Mater. Today 17 (2019) 1–35, https://doi.org/10.1016/j.apmt.2019.06.015.
[29] S. Nagarajan, H. Belaid, C. Pochat-Bohatier, C. Teyssier, I. Iatsunskyi, E. Coy, S. Balme, D. Cornu, P. Miele, N.S. Kalkura, V. Cavaillès, M. Bechelany, Design of boron nitride/gelatin electrospun nanofibers for bone tissue engineering, ACS Appl. Mater. Interfaces 9 (2017) 33695–33706, https://doi.org/10.1021/acsami.7b13199.
[30] O. Graniel, M. Weber, S. Balme, P. Miele, M. Bechelany, Atomic layer deposition for biosensing applications, Biosens. Bioelectron. 122 (2018) 147–159, https://doi.org/10.1016/j.bios.2018.09.038.
[31] M. Pavlenko, E.L. Coy, M. Jancelewicz, K. Załęski, V. Smyntyna, S. Jurga, I. Iatsunskyi, Enhancement of optical and mechanical properties of Si nanopillars by ALD TiO 2 coating, RSC Adv. 6 (2016) 97070–97076, https://doi.org/10.1039/C6RA21742G.
[32] M. Weber, A. Julbe, A. Ayral, P. Miele, M. Bechelany, Atomic layer deposition for membranes: basics, challenges, and opportunities, Chem. Mater. 30 (2018) 7368–7390, https://doi.org/10.1021/acs.chemmater.8b02687.
[33] S. Hober, K. Nord, M. Linhult, Protein A chromatography for antibody purification, J. Chromatogr. B 848 (2007) 40–47, https://doi.org/10.1016/j.jchromb.2006.09.030.
[34] J.A. Libera, J.W. Elam, M.J. Pellin, Conformal ZnO coatings on high surface area silica gel using atomic layer deposition, Thin Solid Films 516 (2008) 6158–6166, https://doi.org/10.1016/j.tsf.2007.11.044.
[35] A.L. Patterson, The Scherrer formula for X-ray particle size determination, Phys. Rev. 56 (1939) 978–982, https://doi.org/10.1103/PhysRev.56.978.
[36] D. Damberga, R. Viter, V. Fedorenko, I. Iatsunskyi, E. Coy, O. Graniel, S. Balme, P. Miele, M. Bechelany, Photoluminescence study of defects in ZnO-coated

polyacrylonitrile nanofibers, J. Phys. Chem. C 124 (2020) 9434–9441, https://doi.org/10.1021/acs.jpcc.0c00326.
[37] M. Baitimirova, R. Viter, J. Andzane, A. van der Lee, D. Voiry, I. Iatsunskyi, E. Coy, L. Mikoliunaite, S. Tumenas, K. Załęski, Z. Balevicius, I. Baleviciute, A. Ramanaviciene, A. Ramanavicius, S. Jurga, D. Erts, M. Bechelany, Tuning of structural and optical properties of graphene/ZnO nanolaminates, J. Phys. Chem. C 120 (2016) 23716–23725, https://doi.org/10.1021/acs.jpcc.6b07221.
[38] L.B.V.S. Garimella, T.K. Dhiman, R. Kumar, A.K. Singh, P.R. Solanki, One-step synthesized ZnO np-based optical sensors for detection of Aldicarb via a photo-induced electron transfer route, ACS Omega. 5 (2020) 2552–2560, https://doi.org/10.1021/acsomega.9b01987.
[39] J.C. Moore, L.R. Covington, R. Stansell, Affect of film thickness on the blue photoluminescence from ZnO, Phys. Status Solidi 209 (2012) 741–745, https://doi.org/10.1002/pssa.201127613.
[40] J. Lee, S. Choi, S.J. Bae, S.M. Yoon, J.S. Choi, M. Yoon, Visible light-sensitive APTES-bound ZnO nanowire toward a potent nanoinjector sensing biomolecules in a living cell, Nanoscale. 5 (2013) 10275, https://doi.org/10.1039/c3nr03042c.
[41] N.S.K. Gunda, M. Singh, L. Norman, K. Kaur, S.K. Mitra, Optimization and characterization of biomolecule immobilization on silicon substrates using (3-aminopropyl)triethoxysilane (APTES) and glutaraldehyde linker, Appl. Surf. Sci. 305 (2014) 522–530, https://doi.org/10.1016/j.apsusc.2014.03.130.
[42] H. Bhardwaj, G. Sumana, C.A. Marquette, A label-free ultrasensitive microfluidic surface Plasmon resonance biosensor for Aflatoxin B1 detection using nanoparticles integrated gold chip, Food Chem. 307 (2020) 125530, https://doi.org/10.1016/j.foodchem.2019.125530.
[43] M. Wei, F. Zhao, Y. Xie, A novel gold nanostars-based fluorescent aptasensor for aflatoxin B1 detection, Talanta. 209 (2020) 120599, https://doi.org/10.1016/j.talanta.2019.120599.
[44] J. Moon, J. Byun, H. Kim, E.-K. Lim, J. Jeong, J. Jung, T. Kang, On-site detection of aflatoxin B1 in grains by a palm-sized surface plasmon resonance sensor, Sensors. 18 (2018) 598, https://doi.org/10.3390/s18020598.
[45] A.F. Alshannaq, J.-H. Yu, A liquid chromatographic method for rapid and sensitive analysis of aflatoxins in laboratory fungal cultures, Toxins (Basel). 12 (2020) 93, https://doi.org/10.3390/toxins12020093.
[46] Z. An, C.-H. Jang, Label-free optical detection of aflatoxin by using a liquid crystal-based immunosensor, Microchem. J. 142 (2018) 335–342, https://doi.org/10.1016/j.microc.2018.07.013.
[47] H. Xie, J. Dong, J. Duan, J. Hou, S. Ai, X. Li, Magnetic nanoparticles-based immunoassay for aflatoxin B1 using porous g-C3N4 nanosheets as fluorescence probes, Sensors Actuators B Chem. 278 (2019) 147–152, https://doi.org/10.1016/j.snb.2018.09.089.
[48] Y. Jia, F. Wu, P. Liu, G. Zhou, B. Yu, X. Lou, F. Xia, A label-free fluorescent aptasensor for the detection of Aflatoxin B1 in food samples using AIEgens and graphene oxide, Talanta. 198 (2019) 71–77, https://doi.org/10.1016/j.talanta.2019.01.078.
[49] T. Sergeyeva, D. Yarynka, E. Piletska, R. Lynnik, O. Zaporozhets, O. Brovko, S. Piletsky, A. El'skaya, Fluorescent sensor systems based on nanostructured polymeric membranes for selective recognition of Aflatoxin B1, Talanta. 175 (2017) 101–107, https://doi.org/10.1016/j.talanta.2017.07.030.
[50] Y. Xiong, K. Pei, Y. Wu, H. Duan, W. Lai, Y. Xiong, Plasmonic ELISA based on enzyme-assisted etching of Au nanorods for the highly sensitive detection of aflatoxin B1 in corn samples, Sensors Actuators B Chem. 267 (2018) 320–327, https://doi.org/10.1016/j.snb.2018.04.027.
[51] J. Lerdsri, W. Chananchana, J. Upan, T. Sridara, J. Jakmunee, Label-free colorimetric aptasensor for rapid detection of aflatoxin B1 by utilizing cationic perylene probe and localized surface plasmon resonance of gold nanoparticles, Sensors Actuators B Chem. 320 (2020) 128356, https://doi.org/10.1016/j.snb.2020.128356.
[52] J. Wu, L. Zeng, N. Li, C. Liu, J. Chen, A wash-free and label-free colorimetric biosensor for naked-eye detection of aflatoxin B1 using G-quadruplex as the signal reporter, Food Chem. 298 (2019) 125034, https://doi.org/10.1016/j.foodchem.2019.125034.
[53] X. Xiong, Y. Li, W. Yuan, Y. Lu, X. Xiong, Y. Li, X. Chen, Y. Liu, Screen printed bipolar electrode for sensitive electrochemiluminescence detection of aflatoxin B1 in agricultural products, Biosens. Bioelectron. 150 (2020) 111873, https://doi.org/10.1016/j.bios.2019.111873.
[54] A. Tereshchenko, V. Smyntyna, A. Ramanavicius, Interaction mechanism between TiO 2 nanostructures and bovine leukemia virus proteins in photoluminescence-based immunosensors, RSC Adv. 8 (2018) 37740–37748, https://doi.org/10.1039/C8RA07347C.
[55] R.B.M. Schasfoort, P. Bergveld, R.P.H. Kooyman, J. Greve, Possibilities and limitations of direct detection of protein charges by means of an immunological field-effect transistor, Anal. Chim. Acta 238 (1990) 323–329, https://doi.org/10.1016/S0003-2670(00)80554-1.
[56] P. Bergveld, A critical evaluation of direct electrical protein detection methods, Biosens. Bioelectron. 6 (1991) 55–72, https://doi.org/10.1016/0956-5663(91)85009-L.
[57] N. Haustein, Ó. Gutiérrez-Sanz, A. Tarasov, Analytical model to describe the effect of polyethylene glycol on ionic screening of analyte charges in transistor-based immunosensing, ACS Sensors. 4 (2019) 874–882, https://doi.org/10.1021/acssensors.8b01515.
[58] H. Ohshima, S. Ohki, Donnan potential and surface potential of a charged membrane, Biophys. J. 47 (1985) 673–678, https://doi.org/10.1016/S0006-3495(85)83963-1.
[59] Z. Zhang, J.T. Yates, Band bending in semiconductors: chemical and physical consequences at surfaces and interfaces, Chem. Rev. 112 (2012) 5520–5551, https://doi.org/10.1021/cr3000626.
[60] W. Yang, J.E. Butler, J.N. Russell, R.J. Hamers, Direct electrical detection of antigen-antibody binding on diamond and silicon substrates using electrical impedance spectroscopy, Analyst. 132 (2007) 296–306, https://doi.org/10.1039/b612201a.
[61] R. Ramales-Valderrama, A. Vázquez-Durán, A. Méndez-Albores, Biosorption of B-aflatoxins using biomasses obtained from formosa firethorn [*Pyracantha koidzumii* (Hayata) Rehder], Toxins (Basel). 8 (2016) 218, https://doi.org/10.3390/toxins8070218.
[62] S. Azizian, S. Eris, L.D. Wilson, Re-evaluation of the century-old Langmuir isotherm for modeling adsorption phenomena in solution, Chem. Phys. 513 (2018) 99–104, https://doi.org/10.1016/j.chemphys.2018.06.022.
[63] I. Baleviciute, V. Ratautaite, A. Ramanaviciene, Z. Balevicius, J. Broeders, D. Croux, M. Mcdonald, F. Vahidpour, R. Thoelen, W. De Ceuninck, K. Haenen, M. Nesladek, A. Reza, A. Ramanavicius, Evaluation of theophylline imprinted polypyrrole film, Synth. Met. 209 (2015) 206–211, https://doi.org/10.1016/j.synthmet.2015.07.021.
[64] Z. Saadi, R. Fazaeli, L. Vafajoo, I. Naser, G. Mohammadi, Promotion of clinoptilolite adsorption for azithromycin antibiotic by Tween 80 and Triton X-100 surface modifiers under batch and fixed-bed processes, Chem. Eng. Commun. 0 (2020) 1–21, https://doi.org/10.1080/00986445.2020.1715955.
[65] M. Haidukowski, E. Casamassima, M.T. Cimmarusti, M.T. Branà, F. Longobardi, P. Acquafredda, A. Logrieco, C. Altomare, Aflatoxin B1-adsorbing capability of Pleurotus eryngii Mycelium: efficiency and modeling of the process, Front. Microbiol. 10 (2019), https://doi.org/10.3389/fmicb.2019.01386.
[66] W.-R. Lim, S.W. Kim, C.-H. Lee, E.-K. Choi, M.H. Oh, S.N. Seo, H.-J. Park, S.-Y. Hamm, Performance of composite mineral adsorbents for removing Cu, Cd, and Pb ions from polluted water, Sci. Rep. 9 (2019) 13598, https://doi.org/10.1038/s41598-019-49857-9.
[67] Q. Luo, J.D. Andrade, Cooperative adsorption of proteins onto hydroxyapatite, J. Colloid Interface Sci. 200 (1998) 104–113, https://doi.org/10.1006/jcis.1997.5364.
[68] H.N. Eisen, F. Karush, Immune tolerance and an extracellular regulatory role for bivalent antibody, Nature. 202 (1964) 677–682, https://doi.org/10.1038/202677a0.
[69] W. Wang, S. Singh, D.L. Zeng, K. King, S. Nema, Antibody structure, instability, and formulation, J. Pharm. Sci. 96 (2007) 1–26, https://doi.org/10.1002/jps.20727.